JOURNAL OF GEOPHYSICAL RESEARCH, VOL. 113, C05018, doi:10.1029/2007JC004390, 2008

Doppler spreading of internal gravity waves by an inertia-wave packet

J. C. Vanderhoff,[1,3] K. K. Nomura,[1] J. W. Rottman,[1] and C. Macaskill[2]

Received 13 June 2007; revised 19 October 2007; accepted 25 January 2008; published 15 May 2008.

[1] Present Doppler-spreading models for the high wave number end of atmospheric and oceanic internal wave spectra either neglect the time dependence of the background long-wave shear entirely, or ignore time-dependent effects in their parameterization of dissipation. Through ray tracing and numerical simulations the Doppler spreading of an idealized interaction between a short internal-wave packet by an inertia-wave packet is examined. The results are sufficient to show that time dependence in the long-wave shear can make a significant difference to short-wave behavior, and will need to be taken into account in future modeling efforts.

Citation: Vanderhoff, J. C., K. K. Nomura, J. W. Rottman, and C. Macaskill (2008), Doppler spreading of internal gravity waves by an inertia-wave packet, *J. Geophys. Res.*, *113*, C05018, doi:10.1029/2007JC004390.

1. Introduction

[2] There is a growing consensus that realistic models of oceanic and atmospheric internal gravity wave spectra need to take account of certain strongly nonlinear effects not included in weakly nonlinear or resonant triad interaction theory. Such strongly nonlinear effects include, first, wave breaking and the resulting turbulence (probably the main cause of wave dissipation) and, second, a class of wave-wave interactions that may be referred to as ''Doppler spreading'', a broadening of the short-wave spectrum due to advection and refraction by a random field of longer waves, especially those of near-inertia intrinsic frequency. The term Doppler spreading was coined by *Hines* [1991], but the ideas go back to *Munk* [1981].

[3] *Hines* [1991] has argued for Doppler spreading as a process of primary importance in accounting for the observed shape at high wave numbers in atmospheric gravity wave spectra, but like *Munk* [1981], assumed that the Doppler spreading could be treated as if the background velocity fields of the larger scale internal waves were steady, allowing the application of standard ideas about wave breaking on approach to critical layers.

[4] The most highly developed and popular model of short internal waves in the deep ocean is due to *Henyey and Pomphrey* [1983], *Henyey et al.* [1986] and *Müller et al.* [1986]. They study the refraction of short internal waves by a broadband (Garrett-Munk) spectrum of larger-scale internal waves. In *Henyey et al.* [1986] the flux of wave-energy refracted toward short vertical scales (5 m wavelength) is converted into a dissipation rate independently of the wave amplitude. Their ray tracings suggest that Doppler spreading is a process of primary importance in accounting for the observed high wave number shape and intensity of internal-wave spectra. The results show reasonable agreement with measurements and recently have been shown to predict the observed latitude dependence of dissipation by *Gregg et al.* [2003].

[5] In addition to the study of a spectrum of long waves, as Hines and Henyey have done, a more detailed approach seeking to understand the interaction of a single short-wave packet and a single long-wave packet was initiated by the ray-tracing study of *Broutman and Young* [1986]. They were motivated in part by the question of how a critical layer interaction would be altered if the background consisted of long internal waves rather than a steady current. Continuing this study, *Broutman et al.* [1997] presented a brief overview of the dynamics of short and long wave interactions. More recently, similar studies were done by *Sartelet* [2003a, 2003b] in the atmospheric context. It is clear from these studies that time dependence of the inertia waves changes the behavior of the interaction from that implied by standard critical layer ideas. For example, the pileup or infinite focusing of ray bundles at critical layers tends to be replaced, almost always, by the formation of caustics. So, it is far from clear why the earlier models based on a steady critical layer interpretation work well at all.

[6] In this paper, we continue to examine single-packet interactions, using numerical models in addition to ray-tracing. In extending the short preliminary paper of *Broutman et al.* [1997], who also combined ray-tracing and numerical models for single-packet interactions, we consider more cases and cover them in greater detail, seeking to understand the dynamics of strong refraction. We use a Fourier spectral numerical model, run at very high vertical resolution to ensure an accurate simulation of the wide range of vertical scales achieved during refraction. The short wave vertical wave number is varied to include the three cases discussed by *Broutman et al.* [1997]. The long waves are of inertial frequency, as there is a strong peaking of observed oceanographic spectra near the inertia frequency, and their amplitudes are also chosen to be representative of observations. In particular we are interested in the spectra

[1]Department of Mechanical and Aerospace Engineering, University of California, San Diego, La Jolla, California, USA.
[2]School of Mathematics and Statistics, University of Sydney, NSW, Australia.
[3]Now at Department of Mechanical Engineering, Brigham Young University, Provo, Utah, USA.

0148-0227/08/2007JC004390$09.00

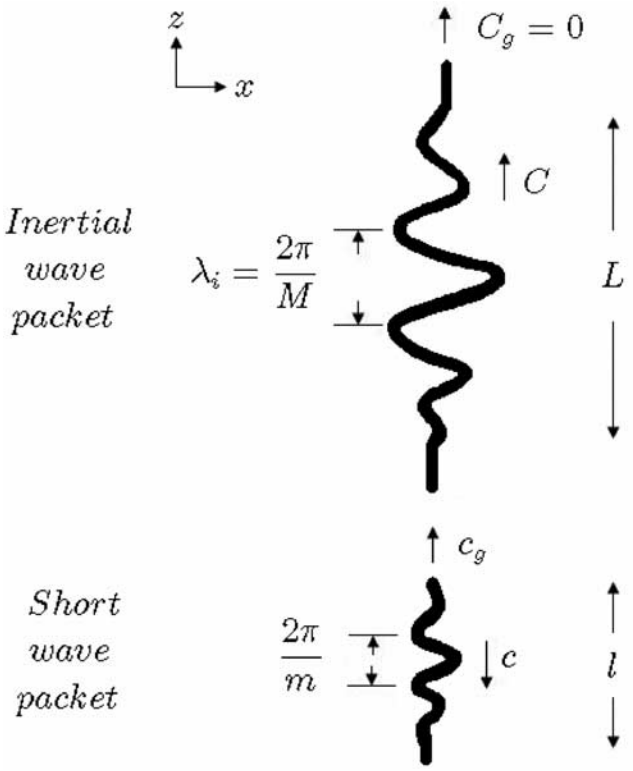

Figure 1. Schematic of a short wave packet approaching an inertia-wave packet with basic parameters shown. (Capital letters denote inertial wave properties).

generated by single-packet interactions, and in understanding the conditions that are most likely to lead to wave breaking.

[7] The results indicate that, contrary to what is assumed in some current models of oceanic internal wave dissipation, steady critical layers are rare in time-dependent shears that are representative of real oceanic flows. In our simulations, the strongest amplification of the short internal waves occurs at caustics. Whether this amplification will lead to breaking depends strongly on the initial amplitude and vertical wave number of the short waves. Therefore we conclude, contrary to Henyey and Hines, that the parameterization of dissipation for short-wave, long-wave interactions does not depend solely on vertical wavelength; there must be an amplitude dependence as well.

[8] In section 2, an idealized model of the interaction of an internal short-wave group with an inertial wave group is formulated. The first part of section 3 contains a brief description of ray theory as it applies to this idealized interaction, assuming that the fluid is Boussinesq, the waves are small amplitude, and the background is slowly varying on the scale of the waves. The following parts of section 3 catalogue the results of the use of ray theory to compute the three main types of interactions first defined by *Broutman et al.* [1997]. Ray theory is a good tool for illustrating the fundamental characteristics of these idealized interactions. In section 4, a fully nonlinear numerical method is used to obtain solutions for the three main types of idealized interactions. These simulations also employ the Boussinesq approximation, but do not require the small amplitude or slowly varying assumptions. We use this nonlinear model to simulate the three basic interactions for more realistic ocean conditions and to compute spectra. In section 5 we discuss how the ideas developed in the previous sections can be applied to the real ocean, and in section 6 we conclude with a summary and some ideas for extending this investigation.

2. The Idealized Problem

[9] We consider the situation in which a single packet of short waves approaches a single packet of inertia waves either from above or below. Figure 1 depicts the initial wave situation with the short wave below the inertia wave in this case. The coordinate system is (x, y, z) with z positive upwards. We assume that the buoyancy frequency N and the Coriolis parameter f are both constant.

[10] The waves of the inertia-wave packet have wave number $\mathbf{K} = (0, 0, M)$, where $M = 2\pi/\lambda_i$ and λ_i is the vertical wavelength of the inertial wave. The corresponding velocity field is a purely horizontal, time-dependent current $\mathbf{u} = (u, v, 0)$ extending infinitely far in the horizontal, but confined in the vertical by a Gaussian envelope:

$$u + iv = u_0\, e^{-z^2/L^2}\, e^{i(Mz - ft)} \tag{1}$$

where L and u_0 are constants, real and complex respectively. The envelope of the inertia-wave packet is stationary, since the group velocity at the inertia frequency is zero, but the phases move vertically through the packet at speed $c = f/M$, assumed positive for the moment. An inertial period is defined as $T_i = 2\pi/f$.

[11] The short waves have wave number $\mathbf{k} = (k, 0, m)$, with k constant, and intrinsic frequency $\hat{\omega}$, where

$$\hat{\omega}^2 = \left(N^2k^2 + f^2m^2\right)/\left(k^2 + m^2\right) \tag{2}$$

which simplifies to

$$\hat{\omega}^2 \approx \frac{N^2k^2}{m^2} \tag{3}$$

when $f^2 \ll \hat{\omega}^2 \ll N^2$. We take k and $\hat{\omega}$ to be positive, and allow m to have either sign. The vertical group velocity $c_g = \partial\hat{\omega}/\partial m$ is negative if m is positive and positive if m is negative.

[12] The vertical displacement of the short waves is $\zeta = \zeta_0 \exp(i\theta)$, from which the wave number and wave frequency are given by $\mathbf{k} = \nabla\theta$ and $\omega = -\theta_t$, respectively, where $\omega = \hat{\omega} + ku$. The wave-energy density E is related to ζ_0 by

$$E = \frac{1}{2}\rho_0\zeta_0^2N^2\left[1 + \left(\frac{fm}{Nk}\right)^2\right] \tag{4}$$

where ρ_0 is the mean density of the fluid. The wave-action density $A = E/\hat{\omega}$.

[13] The numerical simulations are initialized at time $t = 0$ with a short-wave packet whose vertical displacement field $\zeta(x, z, t)$ has the initial form

$$\zeta(x,z,0) = \mathrm{Re}\left\{\zeta_0\, e^{-(z-z_0)^2/\ell^2} e^{i(kx+mz)}\right\} \tag{5}$$

where ℓ and z_0 are real constants and ζ_0 is a complex constant. The initial vertical position z_0 is specified such that the short-wave packet is above the inertia-wave packet if $c_g < 0$, and below it if $c_g > 0$.

[14] For all the results shown in this paper, we use the following parameter values, which are within the range of internal waves in the deep ocean at midlatitudes [see *Pinkel*, 1984]: $M/k = 2$, $\ell/L = 0.75$, $N/(Mu_0) = 2.4$, $N/f = 75$, $M = 2\pi/(100\ \mathrm{m})$, and $f = 10^{-4}\ \mathrm{s}^{-1}$, which yields $u_0 = 0.05\ \mathrm{m\ s}^{-1}$. In the ray-tracing integrations described in section 3 we use $ML = 2\pi$, but for the numerical simulations ray-tracing calculations described section 4 we use $ML = \pi/5$. The larger value is used in section 3 for pedagogical purposes, to illustrate more clearly the nature of the different encounters. The smaller value is used in section 4 because it is more representative of the real ocean. The initial wave steepness of the short waves is specified to be $|\zeta_z| = |m\zeta_0| = 0.1$, where subscript z represents the partial derivative with respect to z. The vertical wave number of the short waves, m, is specified for each case to obtain different values of the vertical group speed.

3. Ray Calculations

3.1. Ray Theory

[15] Using ray theory we can calculate approximately the behavior of the short wave encounter with the inertial wave group. To do this we assume that the inertial wave is both unaffected by the short wave interaction and has a much larger length scale than that of the short wave. Also we assume the short wave is determined by the linear dispersion relation. Then an evolution equation in characteristic form can be found for **k**.

3.1.1. The Ray Equations

[16] The ray-tracing results in this paper are obtained with the following pair of ray equations, for the vertical position of the raypath and the vertical wave number respectively:

$$\frac{dz}{dt} = c_g, \qquad \frac{dm}{dt} = -k\frac{\partial u}{\partial z}. \tag{6}$$

[17] Here $d/dt = \partial/\partial t + c_g\partial/\partial z$. Because the expression (1) has no dependence on x or y, the horizontal components (k, 0) of the wave number of the short waves are conserved along the ray. Thus the constancy of k already assumed is a consistent assumption. To predict wave steepness a set of additional equations based on wave-action conservation is integrated. These equations, which are described by *Broutman* [1986] and here in Appendix A, make consistent allowances for structure near caustics in view of its likely importance for wave-breaking thresholds.

3.1.2. Caustics and Critical Layers

[18] We now turn to the problem of computing short-wave amplitudes at ray singularities known as caustics, which occur in this problem near depths where $c_g = c$. Caustics occur where neighboring rays intersect each other. Here the slowly varying assumption on which ray-tracing is based, breaks down producing infinite amplitudes that do not occur in the full nonlinear problem. We consider two measures of the short-wave amplitude: the wave-steepness, defined as ζ_z, where ζ is the vertical displacement of the short waves; and a component of the wave-induced shear u'_z, where u' is the x-component of the particle velocity of the short waves, and in each measure the subscript z represents the partial derivative with respect to z.

[19] In the ray approximation, the wave-steepness ζ_z has a magnitude $|m\zeta_0|$ that reaches unity when the short waves are about to overturn. For $\hat{\omega} \ll N$, the wave steepness is related to the wave-action density A by

$$|\zeta_z| = k\ (2/\rho_0)^{1/2}\ A^{1/2}\ \hat{\omega}^{-1/2}. \tag{7}$$

This is derived from the dispersion relation and (4). The wave-induced shear u'_z is related to the wave-action density in the ray approximation by

$$|u'_z| = Nk(2/\rho_0)^{1/2}\hat{\omega}^{-1/2}\left(1 - f^2/\hat{\omega}^2\right)^{-1/2}A^{1/2} \tag{8}$$

when $\hat{\omega} \ll N$. The values of $|\zeta_z|$ and $|u'_z|$ are in fact computed in our ray integrations from the more general formulae in which the low frequency approximation $\hat{\omega} \ll N$ is not made. It suffices to plot only $|u'_z|$, since when normalized by their initial values the above solutions for $|u'_z|$ and $|\zeta_z|$ differ only by the multiplicative factor $(1 - f^2/\hat{\omega}^2)^{-1/2}$, which is a function of z.

[20] To determine the corrected value for $|u'_z|$ near the caustic, we start with the caustic correction for the wave-action density A in (B5) of Appendix B, rewritten here for convenience:

$$A_{\max} \approx 1.8 Ri_c^{1/6} A_*. \tag{9}$$

The subscript max denotes the maximum corrected value near the caustic, making the appropriate Airy correction and taking into account the fact that the Airy function reaches its peak on the illuminated side of the caustic. The subscript c denotes the value right at the caustic, and $Ri = N^2/u_z^2$. A_* is the value of A away from the caustic in the direction along the short-wave ray of decreasing vertical group speed c_g. We shall see in the next section that the wave-action density quickly approaches the value of A_* where $c_g \ll c$.

[21] Next we assume that near the caustic, $|u'_z|$ is related to A by the same ray formula (8) that relates $|u'_z|$ and A away from the caustic. The justification behind this assumption is that the Airy function correction valid near caustics associated with $c_g = c$ describes the envelope of the short waves, and within this envelope the short waves are sufficiently slowly varying that the ray-theory relationship between A and $|u'_z|$ still holds to a first approximation. Using (9) to evaluate (8) near the caustic gives

$$|u'_z|_{\max} \sim Nk(2/\rho_0)^{1/2} 1.8^{1/2} Ri_c^{1/12} {A_*}^{1/2} {\hat{\omega}_c}^{-1/2}\left(1 - f^2/{\hat{\omega}_c}^2\right)^{-1/2}. \tag{10}$$

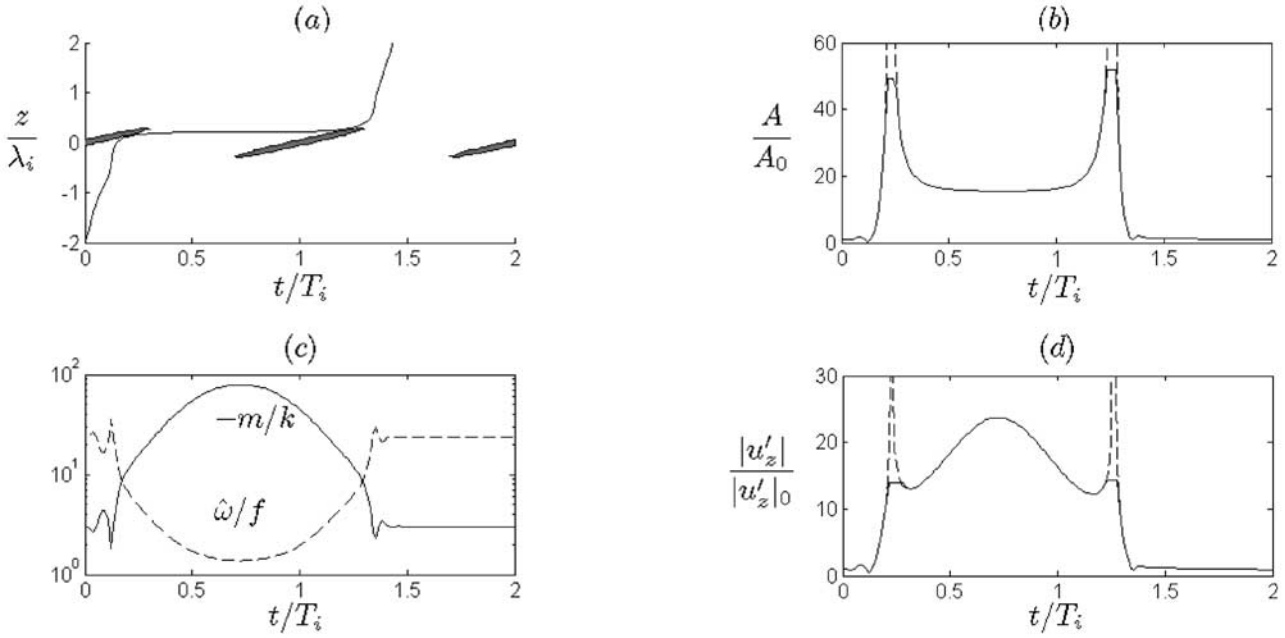

Figure 2. An encounter of the first kind: (a) the raypath, where the boundaries of the shaded, quasi-elliptical regions mark the locations where, at a given instant t, the strong-refraction condition $c_g = c$ can be satisfied (see text); (b) the wave-action density of the short waves, normalized by its initial value, with the dotted line indicating the singular ray solution, and the solid line clipped to indicate the maximum value, $A_{\max}$, near the caustic, where $A_* = 15.5$; (c) the vertical wave number (solid line) and the intrinsic frequency (dashed); (d) the short-wave shear $|u_z'|$ normalized by its initial value, with the dotted line indicating the singular ray solution and the solid line clipped to indicate the maximum amplitude near the caustic. All plots have the same horizontal axis, the time in inertial periods.

Introducing the subscript zero to denote an initial value, we then obtain

$$\frac{|u_z'|_{\max}}{|u_z'|_0} = 1.8^{1/2} Ri_c^{1/12} \left(\frac{A_*}{A_0}\right)^{1/2} \frac{\hat{\omega}_0{}^{1/2}(1 - f^2/\hat{\omega}_0{}^2)^{1/2}}{\hat{\omega}_c{}^{1/2}(1 - f^2/\hat{\omega}_c{}^2)^{1/2}}. \quad (11)$$

[22] All quantities in (11) are easily determined in the numerical ray integrations carried out in the next section. We do not actually match the ray solutions to the Airy function. Instead we simply show plots in which the solution for $|u_z'|$ near the caustic is clipped to the maximum value as calculated from (11).

3.2. Analytic Ray Solutions

[23] An analytic ray solution describing short-wave refraction by inertia waves appears by *Broutman and Young* [1986] and is obtained by letting L approach infinity in (1). The inertia-wave velocity **u** is then purely sinusoidal. In a reference frame moving at the inertial-wave phase speed c, the inertial current appears steady. Solutions then exist for which the short-wave frequency in the inertial-wave reference frame

$$\Omega = \hat{\omega} + ku - cm \quad (12)$$

and the vertical flux of wave-action in the inertial-wave reference frame

$$B = (c_g - c)A \quad (13)$$

are constants.

[24] As described in more detail by *Broutman and Young* [1986] the analytical wave solutions can be divided into two categories: free and trapped. The free solutions either have the short wave group passing through or being passed by successive crests of the inertia wave. The trapped solutions have the short-wave group permanently confined within one wavelength of the inertia-wave, so that there are regions of the inertia-wave train where the short-wave group cannot propagate. The boundaries of these regions are called caustics and are the curves in (t, z) where neighboring rays cross. For our idealized model, caustics occur when

$$c_g = c. \quad (14)$$

[25] The vertical wave number m_c of the short waves at the caustic is

$$m_c \approx -\left(\frac{MkN}{f}\right)^{1/2} = -\left(\frac{kN}{c}\right)^{1/2}. \quad (15)$$

[26] Equation (15) is derived using $c_g \approx kN/m^2$, which follows from (3). In this approximation *Broutman and Young* [1986] find from (12) that the value of u at the caustic is

$$u_c \approx \frac{\Omega}{k} - 2\left(\frac{Nc}{k}\right)^{1/2}. \quad (16)$$

[27] Although substantial refraction occurs in many cases for both the free and trapped solutions, the strongest *focusing* of the short-wave rays occurs at the caustics and these are found only in the trapped solutions. Therefore the trapped solutions are of special interest and are singled out for additional discussion in the next subsection.

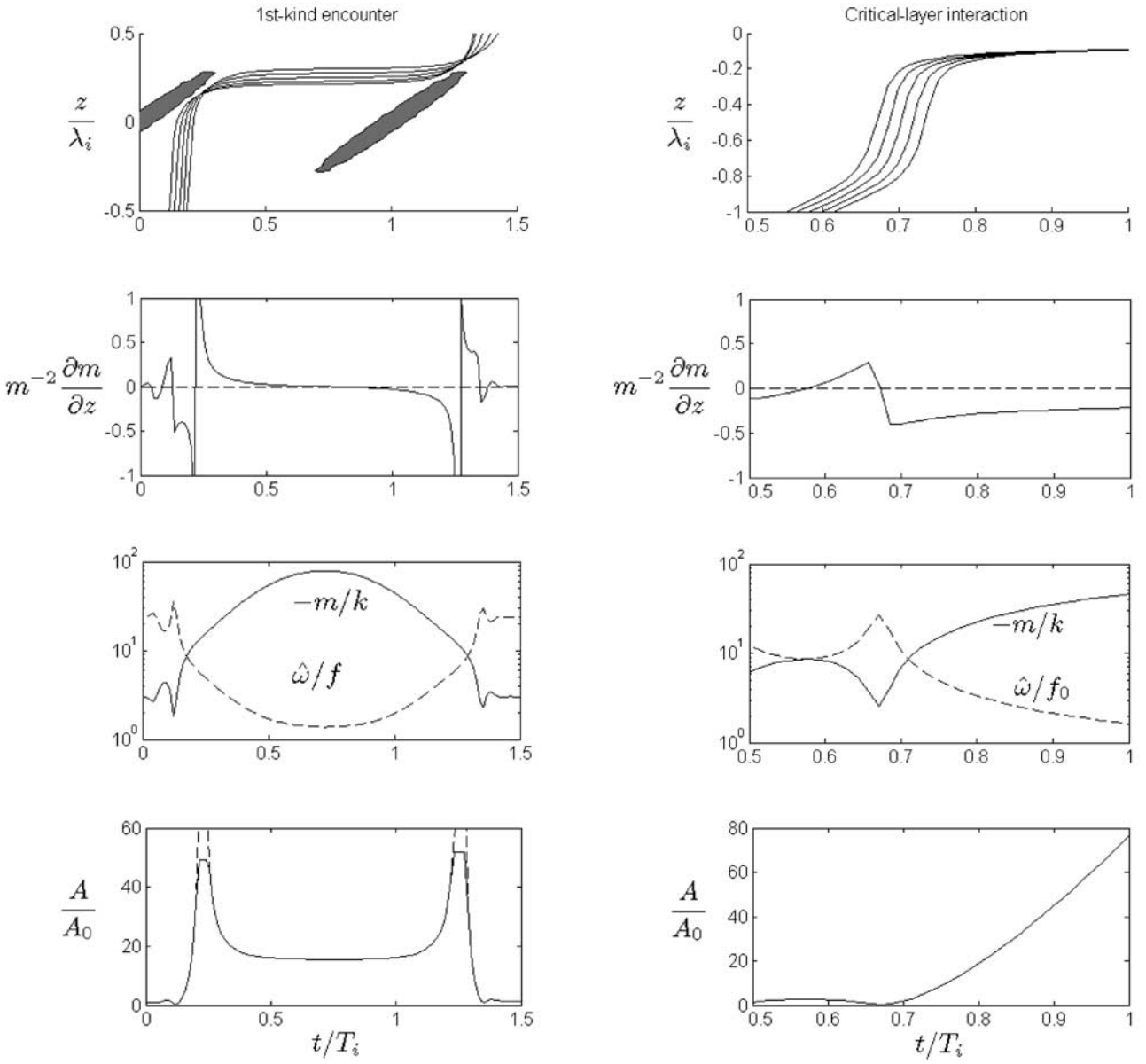

Figure 3. Comparison of the first-kind encounter (left column) with the approach to a critical layer (right column). The plots of $m^{-2}\partial m/\partial z$, m, $\hat{\omega}$, and A are for the first raypath in the corresponding upper plot. For the first-kind encounter, all rays approach the inertia-wave packet with $m/k = -3$. The rays originate from $z = -2\lambda_i$ every 1/60th of an inertial period starting from $t = 0$. The wave number and wave-action density plots are identical to Figure 2 and are redrawn here for convenience. For the critical-layer calculation $m/k = -5$ at the initial time. Since $f = 0$ in the critical-layer calculation, the time axis and intrinsic frequency $\hat{\omega}$ are scaled by $2\pi/f_0$ and f_0 respectively, where $f_0 = N/75$. The rays approach the critical layer from an initial depth of $z = -4\lambda_i$ at intervals of 1/60th of 2 π/f_0, starting with $t = 0$.

[28] A useful result when attempting to extend the above results to encounters with inertia wave packets of finite length can be obtained by noting that typically in our calculations Ω takes approximately the same value before and after the encounter. This implies that large permanent changes in the vertical wave number of the short waves can result from the encounter, as we now show. Let the subscript i denote an initial value, before the encounter, and the subscript f denote a final value, after the encounter. Then since u_i and u_f are zero, outside the envelope of the inertia wave $\Omega_i = \Omega_f$ implies from (12) that

$$\left(\frac{kN}{m_f m_i} + c\right)(m_f - m_i) = 0, \tag{17}$$

where again we have used the approximation (3). Thus $m_f = m_i$ is one possible outcome of the encounter. Alternatively the first factor in (17), using (15) gives

$$\frac{m_f}{m_c} = \frac{m_c}{m_i}. \tag{18}$$

3.3. Numerical Ray Solutions

[29] We have found numerical solutions of the ray equations for a wide variety of short-wave and background inertia wave groups. For a slowly varying packet of inertial waves, these numerical ray integrations indicate that the analytical solutions for the special case of an inertia-wave train provide useful approximations. Caustics coincide approximately with $c_g = c$; and the frequency Ω varies slowly along the ray – more slowly than variations in m or $\hat{\omega}$ [see *Broutman*, 1986, Figures 5 and 6].

[30] Encounters between short waves and inertia waves, in which $c_g = c$ is satisfied at some stage during the encounter, can be divided into three classes depending on the value of c and on the initial value of c_g, say $c_g = c_{g0}$ at $t = 0$. Sample ray calculations for these three classes, which we will refer to as encounters of the first, second and third kinds, are described in the next three subsections.

3.3.1. Encounters of the First Kind $c_{g0} \gg c$

[31] In the first-kind encounter the short-wave group approaches the inertial-wave packet with small vertical wave number and large vertical group velocity. The initial wave number in this example is $m = -3\ k$, giving the initial values $\hat{\omega} \approx 24\ f$ and $c_g \approx 17\ c$. The results of the ray integration are plotted in Figure 2. In each case the time, in inertial periods, is given on the horizontal axis. The depth of the raypath (upper left) is measured in wavelengths of the inertial wave ($\lambda_i = 2\pi/M$) relative to the center of the inertial-wave packet at $z = 0$. The wave-action density A and short-wave shear $|u'_z|$ are normalized by their initial values.

[32] The shaded, quasi-elliptical regions in Figure 2a show the phase propagation of the inertia waves: more precisely, the long axis of each shaded region marks the spacetime locus of a crest or maximum in the u field of the inertia wave. Each quasi-ellipse, i.e., the boundary of each shaded region, marks the approximate depths and times (to leading order in the slow-modulation approximations for the wave packets) at which $c_g = c$ can be satisfied for the given wave parameters.

[33] Since the initial vertical wave number of the short-wave group in this example is $m_i \approx m_c/4$, we expect from (18) that some short-wave groups entering into the inertial-wave packet at a different phase of the inertial wave will emerge from the encounter with their wave number increased by a net factor of about 16. Only in a small number of cases, however, does the final wave number actually increase in magnitude to the larger value whose possibility is predicted by (18). The reason why high-wave number outcomes are uncommon is that at high wave number the short-wave group propagates very slowly and is therefore unlikely to escape from the inertial-wave packet before the next crest of the inertial wave catches up with the short-wave group and refracts the short-wave group to low wave number and fast group velocity [*Broutman and Young*, 1986; *Bruhwiler and Kaper*, 1995]. In most cases, therefore, first-kind encounters conclude with $m_i \approx m_f$. For this example, the final value of the vertical wave number is $m_f = -3.01\ k = 1.003\ m_i$. Permanent changes are more likely in third-kind encounters.

[34] Figure 2 illustrates one of the most important points about the refraction of short internal waves by an inertia wave: the refraction is strongest where $c_g \approx c$, and not (necessarily) where the inertial shear is strongest or where the short-wave wave number is largest. A second important point, to be addressed further in the next section, is that between the caustics in Figure 2, the wave-action density levels off to an approximately constant value, A_*. This is predicted from (13), which indicates that a constant wave-action flux B implies an approximately constant wave-action density A when $c_g \ll c$.

[35] We apply the caustic correction formula (B5), using $A_* \approx 15$ and Ri_c approximately 27 and 35 at the first and second caustics respectively. The corrected value of A near the caustic is then approximately 50. The maximum value for $|u'_z|$ near the caustic, corrected for the ray singularity using (10), is indicated on the plot for $|u'_z|$. The solid line is clipped at this maximum value, while dotted lines represent the singular ray solution.

[36] As regards to its relevance to short-wave dissipation, therefore, this first strong refraction resembles the refraction toward a critical level in steady shear *except* that the steepness is amplified by a finite factor only, reducing though not eliminating the likelihood of wave breaking. Figure 3 contrasts the focusing of rays in a first-kind encounter (left column) with the focusing of rays in a non-rotating critical layer situation of the classic Booker and Bretherton type (right column). The left column has $m/k = -3$ initially and is the same case as shown in Figure 2; the classic critical-layer case, the right column of Figure 3, has $m/k = -5$ initially and $f = 0$ throughout, i.e., $f = 0$ both in (1) and also in the short-wave dynamics. For the first-kind encounter, five rays are shown, each originally separated in time by a sixtieth of an inertia period. After the short-wave rays glance the $c_g = c$ quasi-ellipse, they propagate into a region of stronger shear while refracting to still higher vertical wave number. However, the short-wave focusing weakens as the inertia-wave shear strengthens. This is clear from the plot: the rays become parallel.

[37] As explained by *Broutman et al.* [1997], the wave-action density A becomes approximately constant as the rays become parallel. This can be anticipated theoretically using arguments similar to those of *Broutman and Young* [1986]: in the reference frame moving vertically at the phase speed of the inertia waves the vertical flux of wave-action density, $(c_g - c)A$, is approximately constant, and therefore

$$c_g A \simeq \text{constant} \quad \text{whenever} \quad c_g \gg c \tag{19}$$

$$A \simeq \text{constant} \quad \text{whenever} \quad c_g \ll c. \tag{20}$$

The limit of constant $c_g A$ is relevant to many steady-shear refraction and critical-layer models, and it is this limit that *Hines* [1991] assumes from the very start of his analysis. However, at high vertical wave numbers for which $c_g \ll c$, it is the wave-action density A, not the wave-action flux that becomes constant. This is similar to the steady-shear refraction model proposed by *Phillips* [1966] (included in the first edition only) and related to the original sheared-disturbance theory of *Thomson* [1887], in which the short-wave rays do not converge but instead remain parallel during the refraction.

[38] In a model such as ours, a quantity that measures the degree of ray focusing is $m^{-2}\partial m/\partial z$. This is the fractional

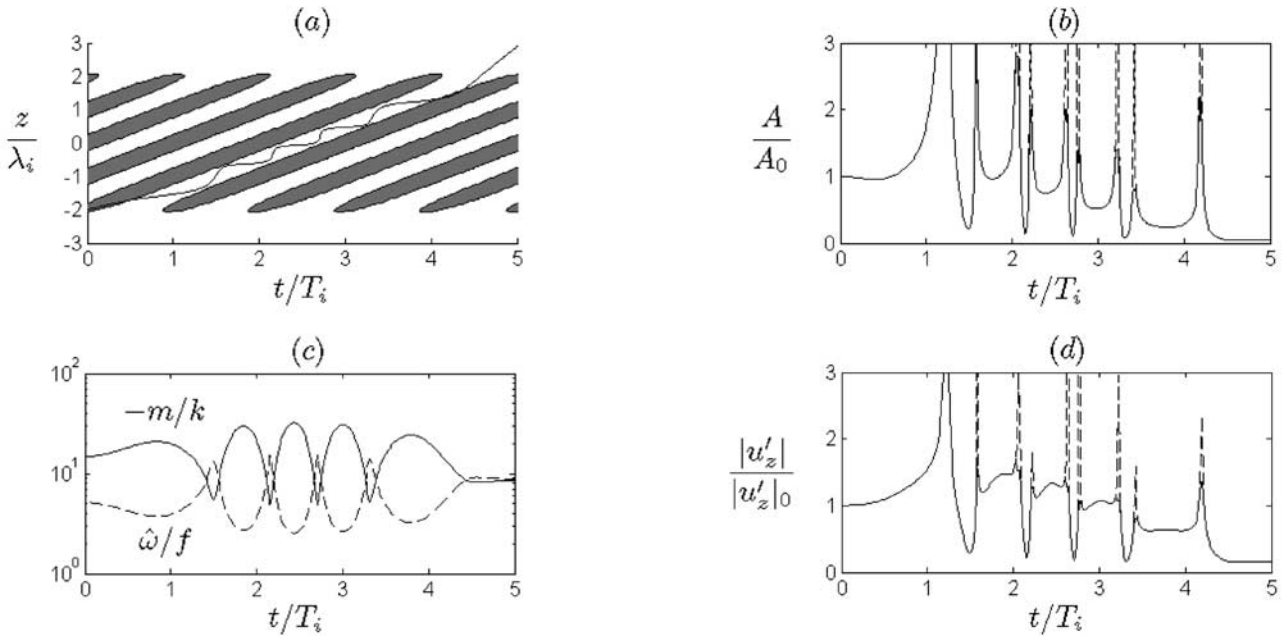

Figure 4. An encounter of the second kind. Plot details are as in Figure 2, but note the different scalings on the time axes, and that, despite appearances, the inertia wave number M and packet envelope scale L are the same; it is only the short-wave parameters and the location of the condition $c_g = c$ that vary. The values for A_* in (b) in order of occurrence are: 0.96, 0.75, 0.51, and 0.23.

change in the vertical wave number over a vertical distance of m^{-1}. Its value can be computed in a ray calculation, and in fact $\partial m/\partial z$ is required anyway to calculate the wave-action density from (A1). When neighboring rays cross at a caustic $\mathrm{m}^{-2}\partial m/\partial z$ diverges. When neighboring rays are parallel $\mathrm{m}^{-2}\partial m/\partial z$ vanishes. Figure 3 includes a plot of $\mathrm{m}^{-2}\partial m/\partial z$, computed numerically for the first ray to reach the caustic in the upper left plot of Figure 3.

[39] Consider again the simple ray model (subsection 3.2) for the case of an inertia wave that is infinite in extent, i.e., with no Gaussian envelope. In the reference frame moving vertically at the phase speed of the inertia wave we find a steady ray solution for $\mathrm{m}^{-2}\partial m/\partial z$. In the limit $\hat{\omega}^2 \ll N^2$ we have from (6), $(c_g - c)\frac{\partial m}{\partial z} = -ku_z$, so that

$$\frac{1}{m^2}\frac{\partial m}{\partial z} = -\frac{u_z}{N}\left[\frac{1}{\left(1-\frac{f^2}{\hat{\omega}^2}\right)^{\frac{1}{2}} - \frac{m^2}{m_c^2}}\right] \tag{21}$$

where we have used $c = c_g(z_c) \approx kN/m_c^2$ to obtain the above expression.

[40] If we first consider a steady shear by letting $c \to 0$ and consequently $m_c \to \infty$, we find that $\mathrm{m}^{-2}\partial m/\partial z$ is proportional to the local shear u_z. Thus if rotation is ignored the rays will approach a critical layer sharply focused if the shear is strong. An example of focused rays approaching a critical layer (without rotation) is shown in the right column of Figure 3. If rotation is included, ray theory itself breaks down in the approach to a critical layer, as $\hat{\omega} \to f$, and ray theory's slowly varying approximation is violated. However, for time-dependent inertial shear, i.e., nonzero c and finite m_c, the combined limit of large vertical wave number m and $\hat{\omega} \to f$ becomes one of vanishing $\mathrm{m}^{-2}\partial m/\partial z$.

[41] The Phillips limit illustrates that strong refraction is not the same as strong focusing. In the Phillips limit (20), unlike limit (19), the wave-energy density (4) decreases as the vertical wave number m increases, as seen in Figure 3. Wave-induced shear and wave steepness increase as m increases, but at a slower rate than they would if the wave-action flux, rather than the wave-action density, were constant. An internal wavefield which obeys the Phillips limit rather than limit (19) may be able to sustain larger amplitudes at lower wave number without saturation at high wave number.

3.3.2. Encounters of the Second Kind $c_{g0} \approx c$

[42] These short waves, with $m/k = -12.25$ initially, satisfy $c_g = c$ immediately upon entering the inertia-wave packet. However, despite this, refraction is weaker than in the first-kind encounter, because the short-wave group becomes trapped around the low-shear trough of the inertia wave midway between two shaded regions. We refer to this case as an *encounter of the second kind*.

[43] The initial condition for the second kind encounter in Figure 4 is $m = m_c \approx -12.25\ k$, or $\hat{\omega} \approx 6.2\ f$. These short waves find caustics immediately upon entering the outer fringes of the inertial-wave packet. Nine caustics occur during the encounter. Toward the center of the inertial-wave packet the quasi-ellipses expand in size, as the caustics migrate toward the nearest trough of the inertial waves. Hence the short waves are trapped by refraction in a region of low inertial shear and experience smaller variations in vertical wave number than those experienced in first-kind and third-kind encounters. The equation (18) suggests that the final wave number should be close to the initial one, as both roots of that equation predict $m_f = m_i$. The ray

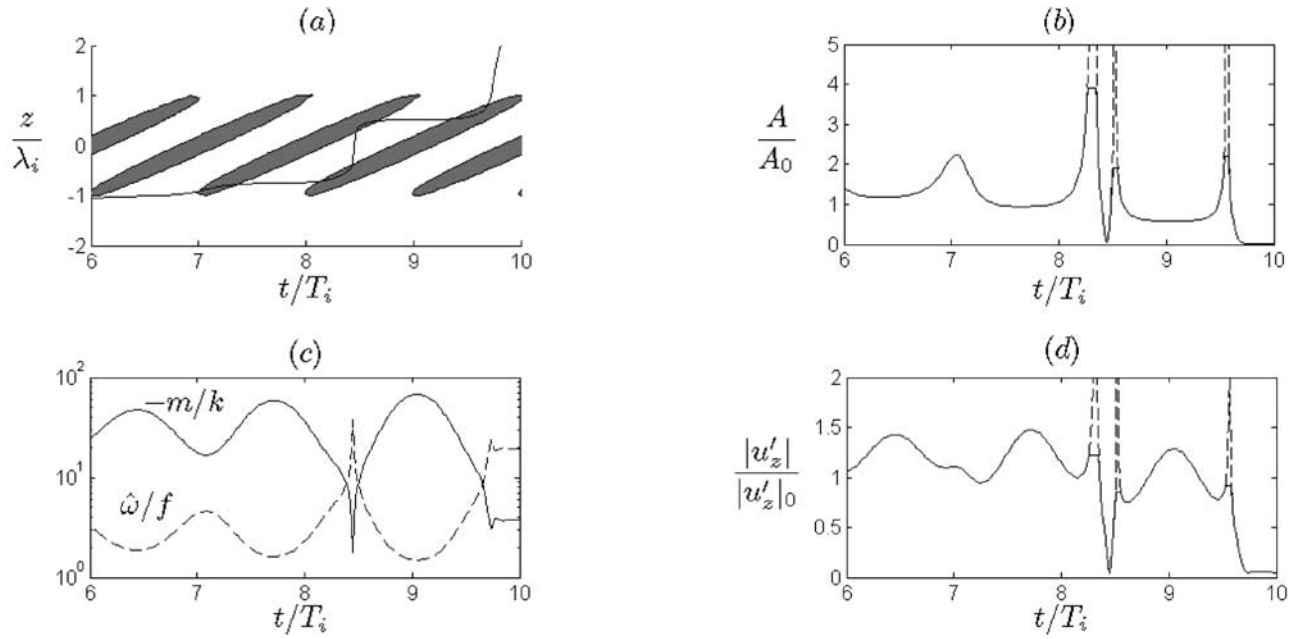

Figure 5. An encounter of the third kind. Plot details are as in Figure 2, but note the different scalings on the time axes, and that, despite appearances, the inertia wave number M and packet envelope scale L are the same; it is only the short-wave parameters and the location of the condition $c_g = c$ that vary. The values for A_* in (b) in order of occurrence are: 0.95, 0.6, and 0.2.

integration gives $m_f = -9.8\ k$, the discrepancy being attributed to a net change in Ω.

3.3.3. Encounters of the Third Kind $c_{g0} \ll c$

[44] In third-kind encounters, the short waves approach the inertial-wave packet very slowly. The ray integration in Figure 5 is initialized with $m/k = -30$ or $\hat{\omega} = 2.7\ f$, implying $c_g \approx 0.17\ c$ The first 6 inertial periods are omitted from the plots.

[45] Despite their slow propagation, the short waves never find critical layers, as they would in a steady current of similar strength. (The horizontal phase speed of the short waves is less than $0.2u_0$ before the encounter.) Nor is there much amplification near the caustics, relative to the initial amplitude, when correction is made to the singular ray solution.

[46] The post-encounter wave number is $m/k \approx -3.6$. Equation (18) predicts $m_f/k \approx -4.3$, but was derived assuming that the initial and final values of Ω are the same, whereas in this example they are different by about a factor of 1.2. This large permanent decrease in the vertical wave number is a common outcome of third-kind encounters, as illustrated in Figures 7 and 9 of *Broutman and Young* [1986], and in many examples provided by *Bruhwiler and Kaper* [1995]. We call this effect the *wave number downshift*. If this were a steady depth-dependent current, instead of a time-dependent one, the wave number downshift would be impossible as it would violate the conservation of the frequency $\hat{\omega} + ku$ along the ray. The conservation of Ω leads instead to a quadratic formula for m, permitting different initial and final wave numbers.

[47] As a result of the wave number downshift, the short-wave group expands in size as it leaves the inertial-wave packet. This is because during the downshift the leading edge of the short-wave group momentarily climbs upward at a faster speed than the trailing edge. Since the integral of the wave-action density over the volume of the short-wave group is constant, the wave-action density itself must decrease, as indicated in Figure 5b. Changes to the inertial waves as the result of this encounter are discussed by *Broutman and Grimshaw* [1988].

[48] Now recall that short waves entering into the first-kind encounter face intense focusing and amplification near their initial caustic. If the short waves are to propagate past the caustic without breaking, and hence persist into the Phillips high-wave number regime, the short waves must initially have very small amplitude with very low frequency. Here is a scenario for how this might happen in the ocean.

[49] Suppose small-amplitude short wave groups are generated at low frequency (where the sources of oceanic internal waves, at least large-scale internal waves, are most energetic), and then interact with large scale internal waves. They initially enter into third-kind encounters, but thereafter are more likely to participate in first-kind encounters because of the wave number downshift, the net decrease in vertical wave number. Thus third-kind encounters may evolve into first-kind encounters. As illustrated in Figure 5 of the present paper, and by *Broutman and Young* [1986], such third-kind encounters culminate with short waves of greatly reduced wave-action density and wave-induced shear. Hence the amplification in the subsequent first-kind encounter would only restore the short waves to their original but small amplitude.

[50] We will refer to those first-kind encounters that evolve from third-kind encounters as *upgraded* first-kind encounters, or simply upgraded encounters. An example is shown in Figure 6. Here the short waves propagate through two vertically separated inertial-wave packets. The lower one, below the horizontal dashed line on the plot of the

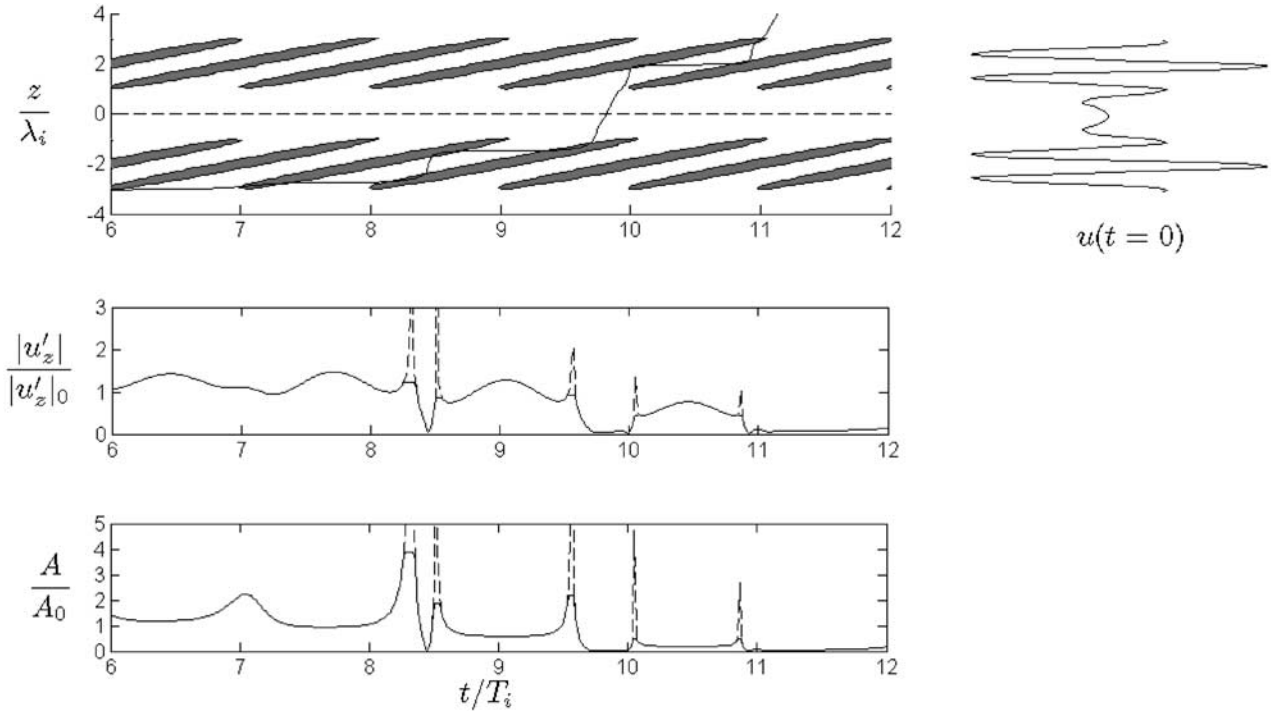

Figure 6. A third-kind encounter followed by an upgraded first-kind encounter. All plots have the same horizontal axis, the time in inertial periods. Top: the raypath, which originates from $z = -4\lambda_i$ at $t = 0$, and the vertical profile of the inertial velocity u at $t = 0$. The lower inertial-wave packet is centered at $z = -2\lambda_i$, and the upper one is centered at $z = 2\lambda_i$. The two inertia waves are the same as shown in Figure 2 The initial wave number of the short waves is $m/k = -30$. Middle: the short-wave shear $|u_z'|$, with the dotted line to indicate the singular ray solution and solid line to indicate the maximum value near the caustic. Bottom: the wave-action density, with the dotted line indicating the singular ray solution and the solid line indicating the maximum value near the caustic.

raypath, is a third-kind encounter; the upper one, above the dashed line, is an upgraded encounter.

4. Numerical Simulations

[51] For comparison with ray theory, which is linear and which assumes, formally, a slowly varying background and slowly modulated wave packets, we now present numerical results obtained by integrating the fully nonlinear inviscid, Boussinesq equations of motion. In their vorticity-stream function form, these are:

$$\frac{\partial^2\psi}{\partial x^2}+\frac{\partial^2\psi}{\partial z^2}=-q \tag{22}$$

$$\frac{\partial q}{\partial t}+J(\psi,q)-\frac{\partial\sigma}{\partial x}-f\frac{\partial v}{\partial z}=0 \tag{23}$$

$$\frac{\partial v}{\partial t}+J(\psi,v)+fu=0 \tag{24}$$

$$\frac{\partial\sigma}{\partial t}+J(\psi,\sigma)-N^2w=0, \tag{25}$$

where q is the y-component of vorticity and $J(\psi, q)$ the Jacobian with respect to (x, z). Here the fluid velocity $\mathbf{u} = (u, v, w)$, and the stream function ψ is defined such that $u = -\partial\psi/\partial z$, $w = \partial\psi/\partial x$, and $q = \partial u/\partial z - \partial w/\partial x$. The scaled density perturbation due to the presence of internal wave motions is $\sigma = g\rho'/\rho_0$ where g is the acceleration due to gravity; the density $\rho = \rho' + \rho_0$, with $\rho_0(z)$ the mean density profile. Because of rotation, there is a nonzero v field, but all variables are assumed to be independent of y.

[52] Periodic boundary conditions are imposed in both the x- and z-directions, and the equations are solved using a Fourier spectral collocation technique with Runge-Kutta time stepping. The computational domain contains one horizontal wavelength of the short waves in the horizontal direction and one vertical wavelength of the inertia waves in the vertical direction.

[53] There are 512 grid points in the vertical direction, but only 8 grid points in the horizontal direction. The low horizontal resolution suffices for this problem (as has been verified by tests at higher resolution) because the short waves, though strongly refracted, are not strongly amplified, and remain well below breaking threshold. The maximum wave-steepness $\partial\zeta/\partial z$ of the short waves over the duration of the simulation is only about twice its maximum value at the initial time, chosen to be 0.1. No viscosity or filtering was necessary to stabilize the calculation. (An initial steepness of 0.2, however, leads to computational instability at this resolution if no filtering is employed.)

[54] Figure 7a shows the perturbation density field computed from the numerical model results as a function of depth and time at a fixed horizontal location. It is an

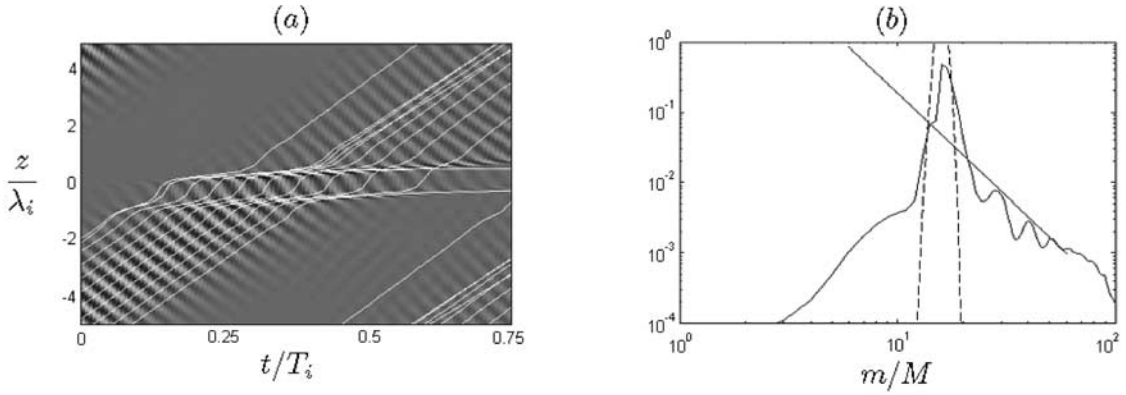

Figure 7. An encounter of the first kind: (a) the perturbation density as a function of depth and time as computed by the spectral numerical method. Overlaid on the plot are raypaths computed as described in section 3; (b) the time-averaged vertical wave number vertical displacement spectrum (solid line). The dashed line is the initial spectrum and the straight line has slope −2.9.

example of a first kind encounter with $m/k = -3$ initially. Raypaths in the *tz* domain were computed for this example and are superimposed on the figure for comparison. The inertia-wave packet does not show up directly in the figure, as there is no corresponding density perturbation. The rays duplicate the the numerical results quite well, showing strong refraction toward high vertical wave number shortly after entering the inertia-wave packet, and no significant net change in vertical wave number after leaving the inertia-wave packet.

[55] Figure 7b shows the vertical-wave number spectrum of the vertical displacement ζ, obtained by averaging spectra over the last half of the simulation. After refraction by the inertia-wave packet, the spectrum of the short-wave packet is broadened such that the slope of the spectrum in the higher wave number region is about −2.9. This is in the range of −2 to −3 slopes of the high-wave number region of spectra typically measured in the ocean. Note that a strong peak in the spectrum remains at the initial vertical wave number, consistent with the observation that many rays exit the interaction with $m_f = m_i$.

[56] Figure 8a shows perturbation density field computed from the numerical models results as a function of depth and time at a fixed horizontal location for a second-kind encounter. In this case the short wave packet has $m/k = -14.7$ initially. The dimensionless inertia-wave packet scale $ML = \pi/5$, or 1/10 of one inertial wavelength, is a smaller value than that used for the ray integrations of the previous section. Raypaths in the *tz* domain were computed for this example and are superimposed on the figure.

[57] The rays duplicate some of the features of the numerical wavefield. The first rays to reach the inertia-wave packet turn upward and then sharply toward the horizontal. The orientation of the phase lines in the numerical solution seems to have the same property, except that some of numerical wavefield reach a turning point point and reflect downward. The rays do not quite reach turning points, which in a *tz* plot would correspond to a vertically oriented ray.

[58] The refraction in this figure seems somewhat stronger than in the earlier ray predictions would indicate for a second encounter. This is probably due to the shorter packet length used in the numerical simulations for the inertia wave. In a second-kind encounter, the short waves avoid strong refraction by gradually moving into the trough of the inertia wave, where the inertia shear is weak. However, if the inertia-wave packet is short, the short waves do not

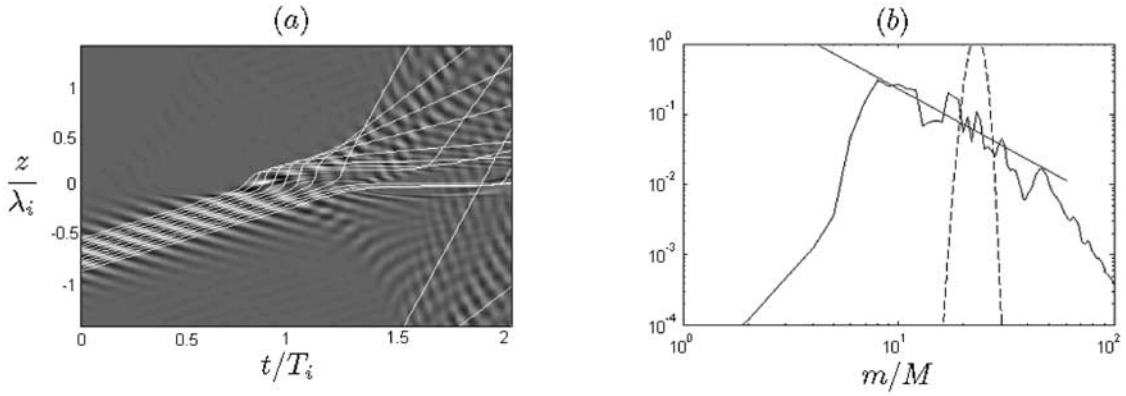

Figure 8. An encounter of the second kind. Plot details are as in Figure 7, but with straight line slope in Figure 8b −1.7.

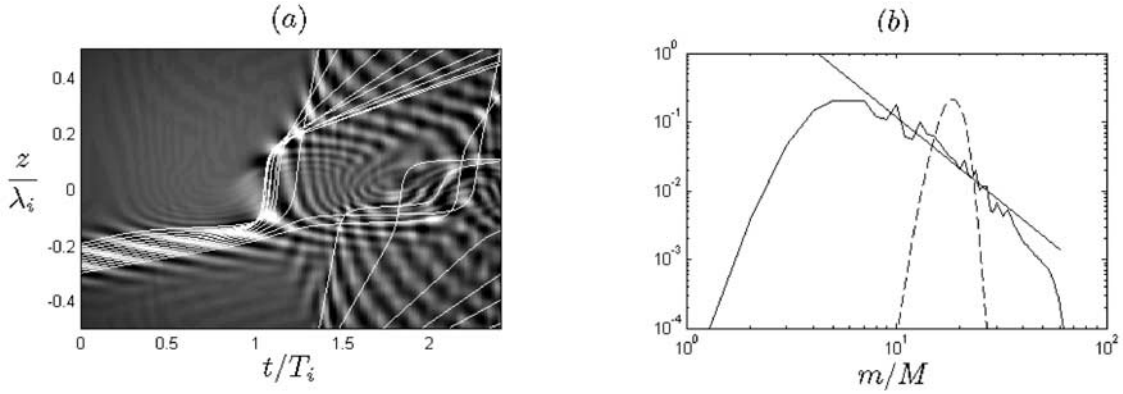

Figure 9. An encounter of the third kind. Plot details are as in Figure 7, but with straight line slope in Figure 9b −2.5.

always reach the trough before encountering relatively large inertia-wave shear.

[59] Note also that the short-wave packet appears to emerge from the inertia-wave packet partially inverted. That is, the first ray to leave the inertia-wave packet is one of the last to enter, and the next rays to exit come from the lower half of the initial short-wave packet.

[60] A graph of the vertical displacement spectrum, computed in a similar manner to that described for the first kind encounter, is shown in, Figure 8b. The plot shows a substantial broadening of the spectrum compared with the initial short-wave spectrum. The broadened spectrum has a vertical wave number region with a slope of about −1.7, and in this case there is no evidence of a peak in the spectrum at the initial wave number of the short-wave packet.

[61] The perturbation density plot of Figure 9a is an example of a third-kind encounter. Initially, the short-wave packet has an initial vertical wave number $m/k = -35$. The inertial wave has the same properties as described above for the second-kind encounter.

[62] The short-wave packet can be seen propagating upwards and then refracting strongly after about one inertia period, in much the same way as in the first strong refraction event seen in Figure 5, i.e., illustrating a $c_g = c$ interaction. Just afterward, some short-wave energy escapes rapidly from the inertia-wave packet, illustrating the permanent decrease in vertical wave number m that is the most striking feature of a third-kind encounter. However, because of the fanning out of the rays above the inertia-wave packet, more of a spread of m values is produced, in this case, than in the case shown in Figure 5. Refraction and the repeated encounters due to the vertically periodic boundary conditions soon spread the short-wave energy throughout the computational domain.

[63] The vertical displacement spectrum for this case is shown in Figure 9b. As in the previous cases, the spectrum is broadened substantially compared with the initial spectrum. Note that a wave number region with slope of about −2.5 is produced within two inertia periods, and in this case there is no evidence of a peak at the initial short-wave vertical wave number. For a computational domain of 100 m depth, the region of −2.5 slope extends from a scale of about 12 m to about 3 m. This was also seen by *Broutman et al.* [1997].

5. Discussion

[64] The ray and numerical simulations summarized here show that short-wave focusing is sharply concentrated around those (time-evolving) depths where $c_g = c$, and that short-wave focusing is relatively weak everywhere else. The calculations have also confirmed that, in order to understand and adequately model the role of Doppler spreading in realistic oceanic and atmospheric spectra, the usual assumptions about critical levels in steady shear need to be treated with caution since they may fail, sometimes drastically, in time-dependent shear. Similar caveats have been put forward by *Eckermann* [1997].

[65] What are the consequences of our conclusions for the interpretation of Henyey's ray simulations? Upgraded encounters may be useful in interpreting the results of *Henyey and Pomphrey* [1983], who ray-trace short-wave groups through a background composed of internal waves of many frequencies and wave numbers, combined with the amplitudes prescribed by the Garrett-Munk internal-wave model [see *Munk*, 1981]. They initialize each short-wave group with high intrinsic frequency and low vertical wave number and terminate the ray integrations if the short-wave group refracts to 5-meter wavelength, supposing critical-layer dissipation in such cases.

[66] It seems likely that the rapid increases in wave number pictured in Henyey and Pomphrey's Figure 6 are associated with the temporary satisfaction of $c_g = c$, involving the short-wave group and some near-inertial component of the background wavefield. If so we would classify them as first-kind encounters. Alternatively, the same results might represent upgraded first-kind encounters. The amplification in a first-kind encounter is strong, upgraded or not, but the likelihood of achieving instability and wave breaking is much less if the encounter is an upgraded one: the short-wave group enters into the upgraded encounter having inherited a very small amplitude from the preceding third-kind encounter. *Flatté et al.* [1985] and *Henyey et al.* [1986] extend the Monte-Carlo ray simulations of *Henyey and Pomphrey* [1983], but they make a key change: the initial horizontal wavelength of the short waves is lengthened to

1000 m, up from 200 m in Henyey and Pomphrey. It is then found, in contrast to Henyey and Pomphrey, that changes in the horizontal wave number of the refracting short waves become as important as changes in the vertical wave number in affecting the spectral transport of wave-action.

[67] In our encounters, increasing the horizontal wavelength of the short waves while keeping the strength of the inertial shear fixed weakens the short-wave refraction in the same way as decreasing the inertial shear while keeping the horizontal wavelength of the short waves fixed [*Broutman and Young*, 1986, Section 2]. Either way, the refracting short waves experience smaller variations in vertical wave number. In the limit of increasing horizontal wavelength, first-kind and third-kind encounters gradually disappear, leaving only second-kind encounters which themselves become progressively weaker. In this limit, only short waves with $m \approx m_c$ before the encounter will ever satisfy $c_g = c$ during the encounter. Thus the relative importance of horizontal wave number variations in the *Flatté et al.* [1985] and *Henyey et al.* [1986] studies may be related to the relative unimportance of the $c_g = c$ condition. As the short waves in the simulations of Flatté et al. and Henyey et al. refract to shorter horizontal wavelength, we would expect $c_g = c$ to be more readily satisfied and consequently the refractive changes in vertical wave number to dominate the refractive changes in horizontal wave number. In this regard, we note that it is only after the short waves refract to the shorter horizontal wavelength of approximately 100–300 m that Henyey et al. find significant refraction to short vertical wavelength, which they associate with dissipation.

[68] A comparison of the encounters with oceanic measurements is suggested by the magnitude of m_c, the vertical wave number at $c_g = c$ and which by (15) is approximately $(kMN/f)^{1/2}$. Suppose we take $N/f = 50$, and use $2\pi/100$ m for both the vertical wave number of the inertial wave M and the horizontal wave number of the short waves k. These values give (ignoring the sign) $m_c \approx 2\pi/14$ m. In estimating m_c, a good indication of N and M is often obtainable from vertical profiles of density and horizontal velocity respectively, but an appropriate value to use here for k is more difficult to assess. Yet there is only a square root dependence on k, and there are lower and upper bounds for k beyond which the short waves propagate either too quickly or too slowly to satisfy $c_g = c$. If we take as a crude lower bound $k \geq N/u_0$ (more like a condition for critical layers), where u_0 is the maximum speed of the inertial current, then

$$m_c \geq M\left(\frac{N}{f}\right)^{1/2}\left(\frac{N}{Mu_0}\right)^{1/2}. \tag{26}$$

Choosing $N/f = 50$ and the minimum Richardson number $(N/Mu_0)^2$ to be $O(1)$, we find that m_c is about seven times the vertical wave number of the background inertial wavefield.

[69] By these estimates m_c falls in the range of wave numbers at which a roll-off in the slope of temperature spectra has often been observed in the ocean [*Gregg et al.*, 1993]. Equation (26) indicates that m_c increases with decreasing latitude and is only weakly dependent upon the total energy level of the internal wavefield, if that total energy is proportional to u_0^2. Both these characteristics are generally consistent with the measurements of *Gregg et al.* [1993]. The steepening slope may thus be related to the importance of parallel-ray refraction at high vertical wave number. In this "Phillips limit", (20) constrains the wave-action density A to be approximately constant. An increase in m, or equivalently a decrease in $\hat{\omega}$ then causes a reduction in the wave-energy density $E = \hat{\omega}A$ of the refracting short waves. The lost wave-energy goes into a mean flow, which takes the form of forced and trailing inertia waves [*Broutman and Grimshaw*, 1988]. Temperature spectra might steepen slightly more than velocity spectra because the short-wave generated inertial waves have no vertical displacement.

[70] The roll-off begins at a vertical scale of 10 m. Is this scale related to the effects of time-dependent shear? For example, do short waves of c_g less than c of the dominant background waves begin to dominate the spectrum at these scales? There is some evidence from the calculations of *Henyey et al.* [1986] that this is the case. If so, and if the short-wave focusing is weak at these scales, then the generation of slowly varying mean flows by the short waves becomes important, and may result in steeper spectral slopes.

[71] What are the consequences of our conclusions for Hines' theory for the high-wave number shape of internal-wave spectra? The context here is the upper atmosphere, where unlike the ocean, the short waves and the long waves are believed to propagate energy predominantly upwards. Hines models upward propagating internal waves only; hence $c_g = c$ interactions do not occur in his model. In such cases, our computations, and those of *Eckermann* [1997] and *Sartelet* [2003a, 2003b], suggest that a steady-shear assumption is likely to lead to an overestimate, perhaps significant, of the strength of the refraction and of the rates of dissipation.

[72] A statistical study done by *Bruhwiler and Kaper* [1995] addresses the question of the high-wave number shape of internal-wave spectra as well. Using ray theory they let a set of short waves with a realistic frequency spectrum propagate through a single inertial wave. The spectrum is accounted for by the number of waves, where each wave has the same initial amplitude. They find a general trend of short waves propagating to higher frequencies, and therefore smaller vertical wave numbers. It is interesting though that they find a flattened short wave frequency spectrum when the initial spectrum had a slope of -2. There is much more statistical work to be done, such as including changes in short wave horizontal wave numbers and propagation through more than one inertial wave.

6. Conclusion

[73] We have extended previous work on the interaction of short internal waves and inertia waves in the following ways: we have included calculations of the wave-induced shear to help indicate the tendency for wavebreaking; we have included numerical simulations for all three encounters, and ray and numerical calculations for encounters in which the short-wave phases and the inertia-wave group propagate in opposite vertical directions; and we have suggested some new consequences of the model for the

oceanic internal wavefield. For example, by introducing the upgraded encounter, we have shown that the strong amplification and steepening of the short waves in a first-kind encounter can be consistent with low levels of short-wave dissipation. Also, we have suggested how short-wave refraction by an inertia wave could lead to a change in slope of measured ocean spectra near 10 m vertical scale. Note that this is a non-dissipative explanation for the slope change.

[74] A number of potentially important effects are omitted from our model. For example, *Sun and Kunze* [1999a, 1999b] found that the inclusion of vertical divergence of the vertical background velocity can enhance the rate at which short waves are refracted to short dissipating scales. A further enhancement can result from short-wave refraction by steady shear. While steady shears are typically weaker than inertia shears in the ocean, they can have an important cumulative effect, as noted by *Buckley et al.* [1999]. Neither steady shear nor vertical background velocity is included in our model.

Appendix A: The Ray Amplitudes

[75] The following three equations furnish the ray amplitude:

$$\frac{d\mathcal{V}}{dt} = \mathcal{V} G_{mm} \frac{\partial m}{\partial z} \tag{A1}$$

$$\frac{d}{dt}\frac{\partial z}{\partial z_0} = G_{mm}\frac{\partial m}{\partial z_0} \tag{A2}$$

$$\frac{d}{dt}\frac{\partial m}{\partial z_0} = -G_{zz}\frac{\partial z}{\partial z_0} \tag{A3}$$

where $\omega(z, t) = G(m, z, t)$. We use G and denote partial derivatives by subscripts when m is to considered with z and t as an independent variable. Since there are frequent caustics, the ray equations are expressed in terms of $\mathcal{V}$, which measures the volume of a ray tube and hence vanishes at the caustic. The quantity $\mathcal{V}$ is essentially the inverse of the wave-action density, the only difference being that $\mathcal{V}$ changes sign each time the ray intersects the caustic. In (A2)–(A3) we treat m and z as functions of their initial position z_0. The solutions of (A2)–(A3) combine to give

$$\frac{\partial m}{\partial z} = \frac{\partial m/\partial z_0}{\partial z/\partial z_0} \tag{A4}$$

which is required to integrate (A1). The full expressions for (A1)–(A3) include terms proportional to G_{mz}, which is zero under present assumptions (as of course is G_x). More information on the amplitude integration can be found by *Broutman* [1986], whose implementation is based on the theory of *Hayes* [1970].

Appendix B: Caustics

[76] The short-wave amplitude near a caustic can be estimated by applying standard Airy-function techniques to the case of a purely sinusoidal inertial wave in which the frequency Ω defined in (12) and the wave-action flux B defined in (13) are constants. Let the ray solution be given in the form

$$a = a_0(z,t)e^{i\theta} \tag{B1}$$

where $\mathbf{k} = \nabla\theta$ and $|a_0^2| = A$, the wave-action density. Let the amplitude near the caustic be of the form $A_0 Ai(\rho)$, where Ai is the Airy function and ρ is a non-dimensional distance from the caustic. Then as shown by *Broutman* [1986]

$$A_0 = |\pi B|^{1/2}\left(\frac{32}{\Omega_{mm}^2\Omega_z}\right)^{1/6} \tag{B2}$$

where Ω_{mm} and Ω_z are evaluated at the caustic. Making use of (3) reduces (B2) to

$$A_0 = \left|\frac{2\pi B}{kN}\right|^{1/2} Ri_c^{1/12}|m_c| \tag{B3}$$

where we define $Ri_c = N^2/u_z c^2$ to be the Richardson number at the caustic.

[77] Though derived for the case of infinite L in (1), (B2) and (B3) probably make reasonable approximations when the inertia waves are localized by an envelope, provided that B and Ω vary slowly, on the envelope scale L. Both B and Ω are easily computed during the ray integration, so this slowly varying assumption can be checked, and if satisfied (B2) can be used to estimate the maximum amplitude near the caustic from the numerical ray solutions.

[78] A simplification of (B3) is appropriate when the refraction is strong enough to make $|m| \gg |m_c|$ on one side of the caustic, as is easily the case in the first- and third-kind encounters presented in section 3. Then $c_g \ll c$ and the conservation of wave-action flux (13) forces A to be approximately constant. Let that value be A_*. Substituting $B \approx cA_*$ in (B3) and using (15) gives a relationship between A_* and the caustic amplitude A_0

$$A_0 = (2\pi)^{1/2} Ri_c^{1/12}\left(A_*\right)^{1/2}. \tag{B4}$$

[79] The Airy function attains the maximum value of approximately 0.54 near the caustic. Thus a caustic-correction formula relating the maximum wave-action density $A_{\max}$ near the caustic to the ray prediction A_* is

$$A_{\max} \approx 1.8 Ri_c^{1/6} A_*. \tag{B5}$$

[80] **Acknowledgments.** We acknowledge extensive discussions with Dave Broutman and M. E. McIntyre. Funding was provided by the National Science Foundation(Grant OCE-0117869) and by the Australian Research Council.

References

Broutman, D. (1986), On internal wave caustics, *J. Phys. Oceanogr.*, *16*, 1625–1635.

Broutman, D., and R. Grimshaw (1988), The energetics of the interaction between short small-amplitude internal waves and inertial waves, *J. Fluid Mech.*, *196*, 93–106.

Broutman, D., and W. R. Young (1986), On the interaction of small-scale oceanic internal waves with near-inertial waves, *J. Fluid Mech.*, *166*, 341–358.

Broutman, D., C. Macaskill, M. E. McIntyre, and J. W. Rottman (1997), On doppler-spreading models of internal waves, *Geophys. Res. Lett.*, *24*(22), 2813–2816.

Bruhwiler, D. L., and T. J. Kaper (1995), Wavenumber transport: Scattering of small scale internal waves by large-scale wavepackets, *J. Fluid Mech.*, *289*, 379–405.

Buckley, G., D. Broutman, J. W. Rottman, and S. Eckermann (1999), On the importance of weak steady shear in the refraction of short internal waves, *Geophys. Res. Lett.*, *26*(18), 2877–2880.

Eckermann, S. D. (1997), Influence of wave propagation on the doppler spreading of atmospheric gravity waves, *J. Atmos. Sci.*, *54*, 2554–2573.

Flatté, S. M., F. Henyey, and J. A. Wright (1985), Eikonal calculations of short-wavelength internal-wave spectra, *J. Geophys. Res.*, *90*(C4), 7265–7272.

Gregg, M. C., D. P. Winkel, and T. B. Sanford (1993), Varieties of fully resolved spectra of vertical shear, *J. Phys. Oceanogr.*, *23*, 124–141.

Gregg, M. C., T. B. Sanford, and D. P. Winkel (2003), Reduced mixing from the breaking of internal waves in equatorial waters, *Nature*, *422*, 513–515.

Hayes, W. D. (1970), Kinematic wave theory, *Proc. R. Soc. London*, *A320*, 209–226.

Henyey, F. S., and N. Pomphrey (1983), Eikonal description of internal wave interactions: A non-diffusive picture of ''induced diffusion'', *Dyn. Atmos. Oceans*, *7*, 189–219.

Henyey, F. S., J. Wright, and S. M. Flatté (1986), Energy and action flow through the internal wave field: An eikonal approach, *J. Geophys. Res.*, *91*(C7), 8487–8495.

Hines, C. O. (1991), The saturation of gravity waves in the middle atmosphere. Part II: Development of doppler-spread theory, *J. Atmos. Sci.*, *48*, 1360–1379.

Müller, P., G. Holloway, F. Henyey, and N. Pomphrey (1986), Nonlinear interactions among internal gravity waves, *Rev. Geophys.*, *24*(3), 493–596.

Munk, W. H. (1981), Internal waves and small-scale processes, in *Evolution of Physical Oceanography: Scientific Surveys in Honor of Henry Stommel*, edited by B. A. Warren and C. H. Wunsch, pp. 264–291, MIT Press, Cambridge, Mass.

Phillips, O. M. (1966), *Dynamics of the Upper Ocean*, 1st ed., pp. 178–185, Cambridge Univ. Press, New York.

Pinkel, R. (1984), Doppler sonar observations of internal waves: The wavenumber-frequency spectrum, *J. Phys. Oceanogr.*, *14*, 1249–1270.

Sartelet, K. N. (2003a), Wave propagation inside an inertia wave. Part I: Role of time dependence and scale separation, *J. Atmos. Sci.*, *60*, 1433–1447.

Sartelet, K. N. (2003b), Wave propagation inside an inertia wave. Part II: Wave breaking, *J. Atmos. Sci.*, *60*, 1448–1455.

Sun, H., and E. Kunze (1999a), Internal wave-wave interactions. Part I: The role of internal wave vertical divergence, *J. Phys. Oceanogr.*, *29*, 2886–2904.

Sun, H., and E. Kunze (1999b), Internal wave-wave interactions. Part II: Spectral energy transfer and turbulence production, *J. Phys. Oceanogr.*, *29*, 2905–2919.

Thomson, W. (1887), Stability of fluid motion – Rectilineal motion of viscous fluid between two parallel planes, *Philos. Mag. A and B*, *24*, 188–196.

C. Macaskill, School of Mathematics and Statistics F07, University of Sydney, NSW 2006, Australia. (c.macaskill@maths.usyd.edu.au)

K. K. Nomura and J. W. Rottman, Department of Mechanical and Aerospace Engineering, University of California, San Diego, 9500 Gilmann Drive, La Jolla, CA 92093-0411, USA. (knomura@ucsd.edu; jrottman@ucsd.edu)

J. C. Vanderhoff, Department of Mechanical Engineering, Brigham Young University, 435V CTB, Provo, UT 84602-4201, USA. (jvanderhoff@byu.edu)